Dynamical evolution of multiple four-wave-mixing processes in an optical fiber

D. L. Hart, Arthur F. Judy, and Rajarshi Roy
School of Physics, Georgia Institute of Technology, Atlanta, Georgia 30332

James W. Beletic
European Southern Observatory, Karl-Sch-Strasse 2, D85748 Garching, Germany

(Received 14 October 1997)

We present unique results of detailed experimental and theoretical investigations of the dynamical evolution of four-wave-mixing spectra in an optical fiber. The experimental measurements probe the evolution of sidebands generated through four-wave mixing as they copropagate with the pumps along the fiber. We find that standard theoretical models are inadequate to predict the experimental results and that it is necessary to modify the approach to modeling the dynamics in two ways. The first modification is to include a pump laser input with multiple longitudinal modes. This reflects the fact that the pump laser fields may actually have internal structure that is not resolved by the spectrometer used and is very small compared to the spacing of the central frequencies of the pump fields. Yet the evolution of the fields is dramatically altered for the sidebands generated by nonlinear processes in the fiber medium. The second is the inclusion of phase noise added along the propagation length; this causes damping of the sideband oscillations. These two modifications lead to excellent agreement of the measurements with numerical predictions of the sideband evolution. [S1063-651X(98)05104-6]

PACS number(s): 42.81.Qb, 05.45.+b, 42.65.Hw

I. INTRODUCTION

The study of wave propagation in a nonlinear dispersive medium, such as an optical fiber, is of interest in many areas of science and engineering. The past few decades have seen enormous growth in the use of optical fibers in communications systems. With this growth, engineers and researchers have been challenged with a wide range of physical phenomena associated with high-intensity light waves propagating in optical fibers. Specifically, some of the interesting characteristics of silica glass, of which fibers are made, are low loss, dispersion, and especially nonlinearity. Since optical fibers have a relatively small cross section, a comparatively small amount of power is required to generate high intensities; thus many nonlinear optical processes are easily observed in the medium [1].

Some of the earliest work in nonlinear fiber optics consisted of both experimental and theoretical investigations of such effects as stimulated Brillouin and Raman scattering [2]. This work stimulated the expansion of research to other nonlinear phenomena, such as four-wave mixing [3], optically induced birefringence [4], self-phase modulation [5], and cross-phase modulation [6]. Advances in communications technology came when researchers realized that the nonlinearity in optical fibers could be exploited. In 1973, Hasegawa and Tappert suggested that optical fibers would support soliton pulses in which the nonlinear effects balance the effects of dispersion [7]. Shortly thereafter, optical solitons were experimentally observed [8]. Technologies using solitons are promising for high-bit-rate optical communication systems [9]. Nonlinear fiber optics has found many uses beyond communications systems, for example, pulse compression [10] and sensor devices [11].

Until recently, communications systems using optical fibers supported one communication channel per fiber. To increase the information capacity of communications systems, engineers have turned to wavelength division multiplexed (WDM) systems in which each communication channel is represented by a unique wavelength. The dominant nonlinear process that limits the information capacity of a WDM system is four-wave mixing. The parameters that set this limit are the power coupled in the fiber and the frequency spacing between adjacent channels.

Nonlinear fiber optics is not only relevant to telecommunications; it is also of great interest in mathematics and physics. The equation that governs wave propagation in a single-mode optical fiber is a nonlinear second-order partial differential equation (the nonlinear Schrödinger equation). This particular equation has been studied extensively for its mathematical properties; for example, its analytic solutions give rise to the possibility of soliton propagation [12]. The nonlinear dynamics accessible in optical fibers is rich and varied and makes an excellent experimental system for the study of many nonlinear phenomena.

In this paper the nonlinear dynamics of four-wave-mixing processes resulting from two waves copropagating in an optical fiber is investigated. Multiple waves at different frequencies copropagating in an optical fiber can interact through the nonlinear susceptibility of the fiber medium to generate new frequencies, sidebands, through four-wave mixing (FWM). Two pump waves at ω_1 and ω_2 input to an optical fiber can generate first-order sidebands at frequencies $\omega_3=2\omega_1-\omega_2$ and $\omega_4=2\omega_2-\omega_1$. Second-order sidebands are found at $\omega_5=2\omega_3-\omega_4$ and $\omega_6=2\omega_4-\omega_3$. The number of sidebands generated is determined by the input power and frequency separation between the pumps; e.g., higher-order sidebands may easily be generated by either increasing the pump power or decreasing the pump detuning.

We present detailed studies of the dynamical evolution of sidebands, generated from two input pump waves at ω_1 and

ω_2, as they propagate along an optical fiber. Previous numerical studies have shown that two critical parameters, the pump power and the frequency separation (detuning) between the pump waves, determine the dynamical evolution of power in the sidebands and the number of sidebands generated in a particular length [13]. Previous theoretical studies have shown interesting and sometimes complex dynamical evolution of the sidebands with length in the fiber [14,15]. Section II reviews the nonlinear dynamical equations used to study the evolution of FWM processes in the optical fiber. There were two sets of equations used throughout this research to model the system; the nonlinear Schrödinger equation (NLSE) [1] and a set of coupled amplitude equations derived from the NLSE [13]. Numerical simulations based on these models that show the sensitivity of the sideband dynamics on the input pump power and frequency detuning are presented. These simulations motivated the initial choice of parameter regimes to investigate in this research.

A unique set of experimental measurements of multiple FWM processes along an optical fiber were performed for this research. The experimental apparatus used to conduct the measurements is presented in Sec. III. The key elements of the system were two tunable dye lasers that were pumped by a frequency-doubled Nd:YAG (neodymium-doped yittrium aluminum garnet) laser, polarization maintaining optical fiber supplied by AT&T Bell Laboratories, a spectrometer, and a high-resolution, low-noise charge coupled device (CCD) camera supplied by Georgia Tech Research Institute (GTRI). The GTRI CCD camera was a critical instrument in the experiments. Standard CCD cameras would have been inadequate to detect very weak sidebands, the regime most of the experiments probed. The experimental results presented here are unique in two ways: First, the GTRI CCD camera allowed for detection of weak (less than 1% of the pump waves) sidebands and second, these are the only detailed measurements tracing the dynamical evolution of the sidebands along a fiber in existence at this time.

Section IV presents the experimental investigation of the dynamical evolution of multiple FWM processes in an optical fiber. Measurements tracing the power in the sidebands along a length of 50 m of fiber are presented. These measurements were done at two input pump powers, which yield different sideband dynamics. The power in the sidebands was observed to evolve periodically with fiber length. However, the periodic evolution appears to damp to a constant value of power for each sideband. Furthermore, each of the sidebands evolves along the fiber with different dynamics. Other studies in which the pump power was varied for a fixed length of fiber are presented as well. The initial growth of the sidebands in the first 5 m of fiber was found to be fairly well predicted by the standard theoretical models. However, for longer lengths, the inadequacy of the models to predict the experimental observations is apparent.

Section V discusses the interpretations of the experimental results. To understand the measurements, the theoretical models are modified by including two effects previously not considered; a pump input with multiple longitudinal modes and phase fluctuations added to the waves as they propagate along the fiber length. The impact of a multimode input is examined and found to dramatically alter the dynamical evolution of the individual sidebands when compared to the standard theory using a single-mode pump input. Weak stochastic phase perturbations, added to the copropagating waves, are also included in the modeling and found to damp the periodic evolution of the power in the sidebands. Neither the relatively straightforward multimode input nor the phase fluctuations that were not so obvious have ever been considered when modeling multiple-wave propagation in an optical fiber. Both effects are found to be critical to understanding and predicting the dynamics of the experimentally observed sideband evolution. This research has probed a very specific regime of a complex nonlinear system. The experimental research pointed to several inadequacies of the standard theoretical models to predict the experimental results. Section VI summarizes the conclusions of this research.

II. THEORETICAL CONSIDERATIONS

Propagation of optical pulses in single-mode optical fibers is described by the well-known nonlinear Schrödinger equation [1]

$$\frac{\partial U}{\partial Z}+\frac{\beta^{(2)}}{T_0^2}\frac{\partial^2 U}{\partial \tau^2}=i\gamma P_0|U|^2U, \tag{1}$$

where U is the complex electric field envelope normalized to the absolute amplitude of the field $\sqrt{P_0}$, P_0 is the total power in the fiber, τ is time normalized to the pulse width and measured in a reference frame moving with the group velocity of the pulse [$\tau=(t-z/v_g)/T_0$], T_0 is the pulse width, and $\beta^{(2)}$ is the group velocity dispersion and is given by the second-order derivative of β, the axial wave vector, with respect to the angular frequency ω_{ave}. The nonlinearity coefficient γ is given by the relationship

$$\gamma=\frac{\omega_{\text{ave}}n_2^1}{cA_{\text{eff}}}, \tag{2}$$

where A_{eff} is the effective core area of the fiber determined by the size of the fundamental mode, n_2^1 is the Kerr coefficient for the intensity-dependent refractive index, and ω_{ave} is the average angular frequency of the wave envelope [1].

In order to obtain the nonlinear Schrödinger equation (1), several assumptions are made. One assumption is an instantaneous nonlinear response of the medium. This is valid for pulses longer than 100 fs since the third-order susceptibility of the medium $\chi^{(3)}$ has electronic contributions on the 1–10 fs time scale [1]. The experimental research used relatively long pulses $\sim$5 ns. The slowly varying envelope approximation is also used where the second-order derivative of the field with respect to the length is neglected. This assumes that the change in slope of the field envelope over a distance of one wavelength is small compared to the slope of the field envelope itself. The optical field is assumed to maintain its polarization along the fiber and thus the scalar form of the NLSE (1). This is justified for the experiments presented here since linearly polarized light from the lasers was propagated with the polarization aligned along one of the principal axes of a polarization preserving fiber (Sec. III). The axial wave vector $\beta(\omega)$ is approximated by a Taylor-series expansion. For wavelengths near the zero dispersion regime ($\lambda \sim 1.3\ \mu$m), where $\beta^{(2)}$ approaches zero, higher-order terms

from the Taylor series need to be included. The experiments in this research were performed in the visible regime ($\lambda \sim 633$ nm), thus only terms up to $\beta^{(2)}$ were retained. The linear fiber loss is also assumed to be negligible. This is justified for the wavelength regime and fiber lengths ($L < 50$ m) investigated since the loss is approximately 6 dB/km at $\lambda \sim 633$ nm, which amounts to less than 1% loss over 50 m.

There are two wavelength regimes of interest in optical fibers, the anomalous dispersion ($\lambda > \lambda_0$) and the normal dispersion ($\lambda < \lambda_0$) regimes, where the zero dispersion wavelength λ_0 can range from 1.3 to 1.58 μm. The experiments presented here were performed in the normal dispersion regime. However, the integrability of the NLSE gives rise to interesting solutions in the form of solitons in both regimes. Soliton propagation occurs when the fiber nonlinearity balances the effect of dispersion and the pulse propagates without dispersive broadening. In the anomalous dispersion regime ($\beta^{(2)} < 0$) the fundamental soliton solution of the NLSE is in the form of hyperbolic secant pulses [1,12]. In the normal dispersion regime ($\beta^{(2)} > 0$) the fundamental soliton solution is in the form of a hyperbolic tangent, giving rise to dark solitons or dips in a continuous-wave background [1,16]. In the context of the experiments presented, in the normal dispersion regime with finite width pulses, a carrier pulse of finite width may support relatively stable propagation of dark pulses for short distances [16]. These are not ''proper'' dark solitons however; the distance of stable propagation decreases with decreasing carrier width.

The split step Fourier method (SSFM), a pseudospectral technique, was used in this research [17]. Specifically, a symmetrized form of the SSFM was used [1] and the fast Fourier transform (FFT) routines were obtained from the IMSL mathematical libraries. An advantage of using the NLSE in the four-wave-mixing problem is that integration is reduced to using the FFT. Modeling four-wave-mixing processes, for example, with a dual frequency input, the total complex field is represented by U, the field envelope, and all frequency components are propagated using the single NLSE. However, care must be taken under conditions where many orders of sidebands are generated. As the number of sidebands increases, the size of the FFT must necessarily be increased.

For long pulses or continuous-wave input, assuming monochromatic waves, the coupled amplitude equations for the pump waves and sidebands derived from the wave equation [13] are written below, normalizing all of the complex field amplitudes to the absolute value of the total amplitude of the pumps with average frequency ω_{ave} (which has total power P_0 at the input end of the fiber)

$$\frac{dU_j}{dz} = i\gamma P\left\{\left(|U_j|^2 + 2\sum_{k\neq j}|U_k|^2\right)U_j + \sum_{k,m,n} d_{kmn}U_kU_mU_n^* e^{\Delta\beta_{kmn}}\right\}, \tag{3}$$

where $j,k,m,n = 1,2,3,4,\ldots$ and $k,m \neq n$. Here Σ_{kmn} denotes the permutations of the indices k, m, and n such that $\omega_k + \omega_m - \omega_n = \omega_j$, and the quantity $\Delta\beta_{kmn} = \beta_k + \beta_m - \beta_n - \beta_j$ is the axial wave-vector mismatch. The quantity d_{kmn} is a degeneracy factor that is unity when $k = m$ and 2 when $k \neq$ m. The nonlinearity coefficient γ is given in Eq. (2). Comparing the coupled amplitude equations (3) with the NLSE (1), the contributions to the evolution of the field U_j are now separated into three sets of terms. On the right-hand side of Eq. (3), from right to left, the contributions are due to self-phase modulation, cross-phase modulation, and FWM.

The linear mismatches $\Delta\beta_{kmn}$ are simplified using the approximation that the material part of the index difference dominates the mismatch and the waveguiding contribution can be neglected. This approximation is justified for the frequency separations in these experiments since the v number characterizing the single transverse mode changes by less than 1% over the entire range of frequencies considered. By using the frequency relationships between the peaks and expanding the propagation constants β_j in a Taylor series about the average frequency ω_{ave}, all the mismatches are found to be integer multiples of the quantity $\Delta\kappa = \Omega^2\beta^{(2)}$, where Ω is the frequency difference, or detuning, between the two pump waves and $\beta^{(2)}$ is the group velocity dispersion [18]. These amplitude equations can be solved numerically and the power in each frequency component obtained as a function of distance along the fiber.

Choosing the scaled powers of the waves to be $\rho_m = |U_m|^2$, in Ref. [18] it was shown that Eq. (3) displays power conservation, as is expected. It was also shown that another conserved quantity

$$C(z) = [\rho_1(z) - \rho_2(z)] + 3[\rho_3(z) - \rho_4(z)] + 5[\rho_5(z) - \rho_6(z)] \tag{4}$$

is obtained for the multiple four-wave-mixing processes that occur within the fiber. It was shown in [18] that the conservation of power and Eq. (4) are the only two conservation relations that involve linear combinations of the powers in the different frequency components. This relation holds at any distance z of propagation in the nonlinear medium and connects the asymmetries of the pump waves and sidebands. A more generalized form of Eq. (4) has been derived from the NLSE and is presented in Ref. [19]. Equation (4) has been verified experimentally for relatively short fiber lengths of less than 2 m (see Ref. [19]). The conservation of asymmetry [Eq. (4)] was used in all of the experimental measurements as a sensitive test for other competing processes not included in the models, for example, stimulated Raman scattering.

The initial parameter regime chosen for the experiments came from numerical simulations of the equations presented above. The dynamics of these equations for multiple waves copropagating in a fiber have been studied numerically for long fiber lengths [14,20]; however, experimental work has been limited to a few meters [13,15]. As the sidebands evolve along the fiber, there is an exchange of power between the pumps and sidebands, the dynamics of which are determined by the phase mismatch between the copropagating waves. The two key experimental parameters for a given optical fiber and wavelength regime that determine the dynamics of the power exchange are the pump detuning and the total input power. This can be seen in Eq. (3), where all terms on the right-hand side are multiplied by P_0 and the FWM terms include oscillating terms with the argument pro-

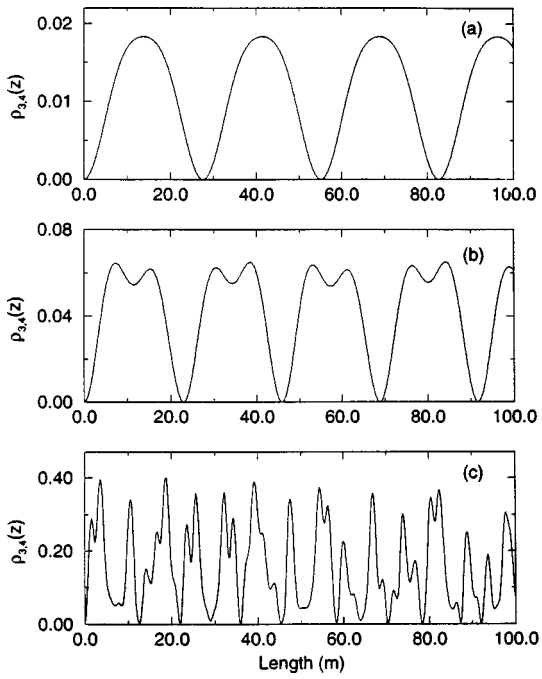

FIG. 1. Dynamical evolution of first-order sidebands as a function of the fiber length for $\Omega = 300$ GHz and input pump powers of (a) 2 W, (b) 6 W, and (c) 50 W. Note the different scales of each vertical axis.

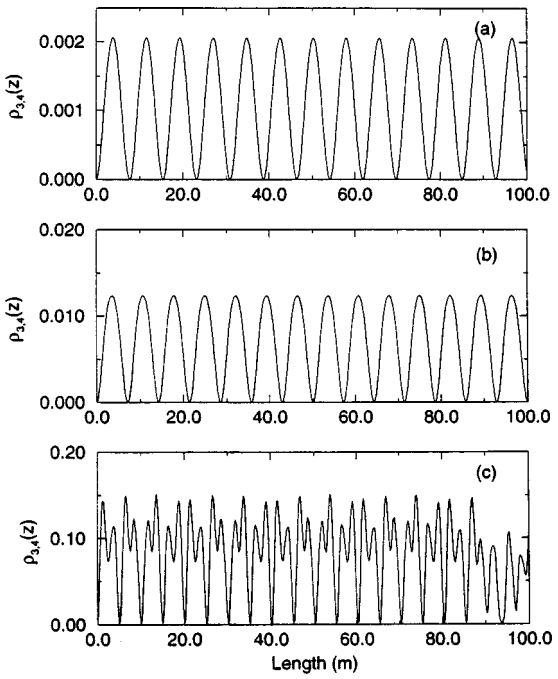

FIG. 2. Dynamical evolution of first-order sidebands as a function of the fiber length for $\Omega = 600$ GHz and input pump powers of (a) 2 W, (b) 6 W, and (c) 50 W. Note the different scales of each vertical axis.

portional to Ω^2. The FWM strength and dynamics are very sensitive to the pump detuning as well as γ and $\beta^{(2)}$. The values used for $\beta^{(2)}$ and γ are same throughout this research, $\beta^{(2)} = 55$ ps^2/km and $\gamma = 0.019$ W^{-1} m^{-1}, and are consistent with the experimental regimes explored later in this paper.

To investigate the dependence of the evolution of the power in the first-order sidebands [$\rho_3(z)$ and $\rho_4(z)$] on the pump power and detuning, the coupled amplitude equations are numerically solved using a fourth-order Runge-Kutta algorithm [21]. A comparison between the power in the sidebands predicted by the NLSE and the coupled amplitude equations was made as a check on the numerical simulations. Simulations based on the NLSE with a continuous-wave (cw) input and the coupled amplitude equations were performed and compared. The comparisons yielded the same predictions for the evolution of the power in the sidebands. However, a comparison of the NLSE using a Gaussian pulse input with either the continuous-wave input or the coupled amplitude equations showed a discrepancy between the models. The power generated in the first-order sideband was found to be higher using the cw input than with the pulse input. It was found necessary to include a scale factor in the cw models, where $\gamma P_0 \rightarrow \zeta \gamma P_0$ with $\zeta = 0.735$. The value of ζ was determined by comparing predictions from the NLSE for a Gaussian pulse input with a continuous-wave input. Intuitively, as the pulse width approaches infinity, the cw and pulse inputs should agree. However, there is no analytic form for estimating this scale factor. Independent studies have also been performed comparing various pulse shapes, input to the NLSE with the cw input, confirming the discrepancy between the two types of input.

The sensitivity of the sideband dynamics on the pump power is illustrated in Fig. 1. The first-order sideband evolution along 100 m of fiber for a detuning of 300 GHz and different input pump powers is plotted in Fig. 1 for (a) 2 W, (b) 6 W, and (c) 50 W. The coupled amplitude equations were truncated to six waves, including up to second-order sidebands. In Fig. 1(a) the input power is low, generating relatively weak first-order sidebands, and the pumps and sidebands exchange power periodically along the fiber. Using an undepleted pump approximation, Eq. (3) has an analytic solution, which shows that the power in the first-order sidebands evolves as a sinusoid as a function of length [22]. In Figs. 1(b) and 1(c), as the pump input power is increased, higher-order sidebands are generated and the power exchange between the pumps and sidebands becomes increasingly complex. In fact, the equations when truncated to include just a few orders of sidebands exhibit chaotic dynamics at high pump powers [13]. However, the NLSE is integrable and does not exhibit chaos. In the case of the coupled amplitude equations the apparent chaos is induced by truncating the equations to include only a few frequency components [14].

Doubling the pump detuning to $\Omega = 600$ GHz, the phase mismatch is increased by a factor of 4. As the phase mismatch increases the efficiency of power conversion from the pumps to the sidebands decreases. The evolution of the first-order sidebands with length in the fiber for a detuning of 600 GHz is shown in Fig. 2 with pump input power levels of (a) 2 W, (b) 6 W, and (c) 50 W. Comparing the evolution with a pump input of 2 W, by doubling the detuning the maximum power in the first-order sidebands is decreased by a factor of 10 [Figs. 1(a) and 2(a)]. The period of the power exchange between the sidebands and pumps has also increased. In Figs. 2(b) and 2(c) it takes much higher powers to generate higher-order sidebands that impact the dynamics of the first-order sidebands. Thus, increasing the detuning decreases the efficiency of the four-wave-mixing power conversion. In-

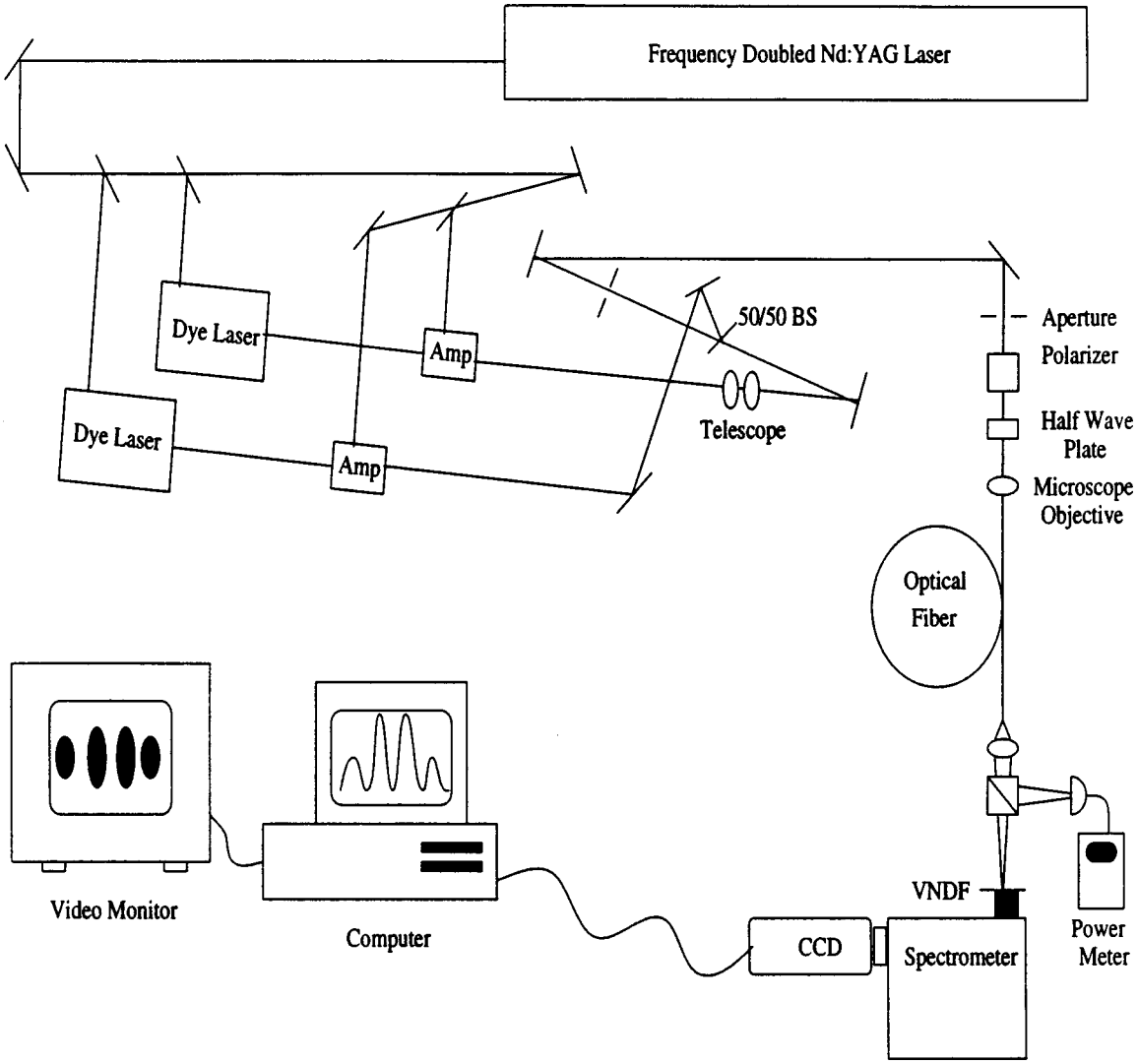

FIG. 3. Experimental setup used to investigate four-wave mixing in an optical fiber. BS denotes beam splitter.

creasing the pump power increases the number of sidebands generated and thus the dynamics becomes more complex.

III. EXPERIMENTAL APPARATUS AND TECHNIQUE

The entire experimental setup used to study multiple four-wave-mixing processes along a length of optical fiber is shown in Fig. 3. The laser system consists of two Littman-type tunable dye lasers, pumped by the second harmonic of a Q-switched frequency-doubled Nd:YAG laser. Pulses that are ~ 5 ns (full width at half maximum) in length are generated. The outputs from the two dye lasers ($\lambda \sim 633$ nm) are amplified and then passed through the appropriate delays to ensure temporal overlap of the pulses at the input to the optical fiber. The telescope in the path of one laser controls the spot size and thus the coupling efficiency, so that the relative power of the two lasers coupled into the fiber can be adjusted to the desired value. The two apertures ensure nearly collinear propagation of the two beams. The light is coupled into a single-mode polarization maintaining optical fiber, after passage through a polarizer and half wave plate. The polarizer at the input to the fiber produces linearly polarized light while the half wave plate rotates the polarization of the light to coincide with a principal axis of the birefringent fiber. The fiber chosen for the experiments was developed by AT&T as an experimental fiber. The fiber is single mode at 633 nm and polarization maintaining. The AT&T fiber achieves high birefringence by deforming a circular fiber preform so that it is rectangular in shape, the cladding is elliptical, and the core is circular [23]. This fiber has a core diameter of 4 μm with a birefringence of 2.7×10^{-4}.

A beam-splitter cube, at the fiber output, is used to direct half of the light to an optical power meter to monitor the power in the pulses while the other half is input to a grating spectrometer. A computer-controlled video camera is mounted on an output port of the spectrometer with a variable neutral density filter (VNDF) placed at the input port to regulate the amount of light incident on the camera. Spectra for individual pulses are digitized and stored in the memory of a microcomputer and a video monitor is used to display each spectrum.

For the experiments presented in this paper, images of the fiber output spectra were captured using a system based on advanced high-speed, low-noise, and high-resolution CCD technology. The system uses a scientific CCD device developed by MIT Lincoln Laboratories [24]. The CCD device is

backside illuminated with 420×420 pixels/frame. To increase the readout rate, there is a separate frame storage region that allows one image to be read as the next one is integrated. Each pixel has a dimension of $27\times27\ \mu m^2$ with a full well depth or charge holding capacity of 100 000 electrons. Pixel nonuniformity has been measured to be 6% peak to peak for similar backside illuminated devices made by MIT Lincoln Laboratories [25]. The advantage of illuminating the CCD from the backside is that the quantum efficiency (QE) is high; for this device the peak QE is 90% near 600 nm. The CCD chip incorporates an on-chip readout amplifier, which is the dominant source of noise in the device.

The camera system was built at GTRI for use in low-light-level astronomical imaging [26]. External to the CCD chip is a 14-bit analog to digital converter and controlling electronics for the CCD that run at a maximum rate of 1 Mpixel/sec. Using the full 420×420 array, this translates to ~5 frames/s. The external electronics incorporate low-noise design techniques such that the system noise is limited by the readout noise from the amplifier on the CCD chip. The CCD is liquid-nitrogen cooled to $-50\,^{\circ}C$, reducing the dark current to 0.04 electrons per pixel (at room temperature the dark current ~700 electrons per pixel). The minimum readout noise from the on-chip amplifier is 7.2 electrons per pixel rms at $-50\,^{\circ}C$ [26].

The camera system is controlled using a Macintosh computer running Labview control software. This software controls a Pulse Instruments PI5800A data generator. The PI5800A generates signals on 16 parallel programmable lines that control the camera. From the camera there is a fiber optic data link that transmits up to 8.3 Mbyte/s. The data are then stored in a high-speed 32 Mbyte ram buffer. From the buffer the data may be either stored on a high-speed video recorder, which runs as fast as 4 Mbytes/s, or for small files it may be stored to a hard disk, which is limited by the input-output ports of the computer system. Programs in Labview were developed with the capability to select a subarray at any location on the chip. For example, in the experiments presented here, a subarray of 10×256 pixels near the center of the chip was chosen. This decreases the size of required data storage and increases the maximum number of frames per second. In these experiments the frame rate is limited to the 10-Hz repetition rate of the Nd:YAG laser system. To achieve the slow rates the camera hardware is programmed to run at 10 Hz and a clock signal is generated that is used to control the laser system through the oscillator sync input. The resolution of the camera-spectrometer system is approximately 43 GHz and is limited by the resolution of the CCD.

The data acquisition method used in this research was to collect output spectra using the GTR1 CCD. The pump lasers fluctuate from shot to shot. For statistical analysis, a total of many spectra for each data point are collected. Typically, 400 independent spectra are captured for each pump propagating alone in the fiber and the two pumps copropagating (FWM). The power in the individual sidebands is measured as a fraction of the total power, normalized to unity, in the fiber, and the total input power is determined based on measurements of each individual pump propagating alone in the fiber. Quantitative measurements are then made of the power in the pumps and sidebands, generated by

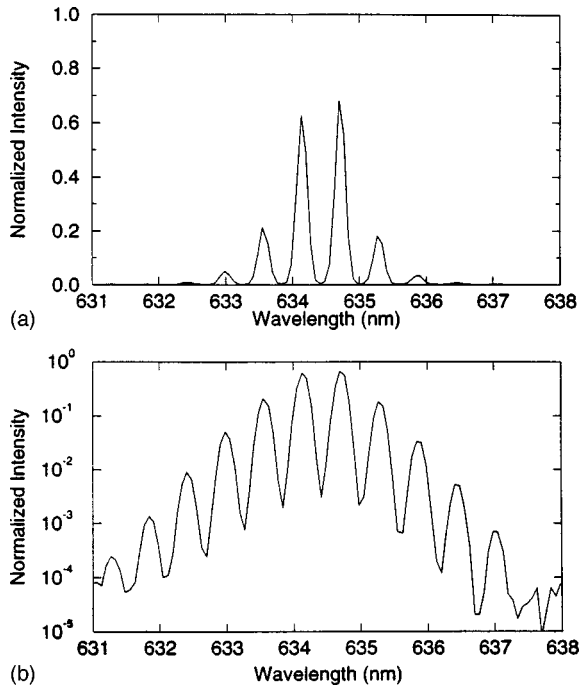

FIG. 4. Experimental FWM output spectrum plotted on (a) a linear scale and (b) a logarithmic scale.

FWM. Prior to data acquisition a set of ''dark'' frames (a set of frames with no light incident on the detector) is collected. An average dark frame is found and then subsequently used to remove the camera bias from the data frames using pixel by pixel subtraction. The power in each frequency component is distributed symmetrically about a central peak for that component. To calculate the power in the pumps and sidebands, we developed software to find the locations of the peaks in the spectrum and the power in each frequency component in two ways. The first is to take a linear cross section along one row and integrate the power in each frequency component. The second is to integrate the power in the full distribution for each component. The second method is insensitive to horizontal misalignment of the CCD detector with respect to the spectrometer. Both methods were employed in this research and agreed closely throughout. Quantitative values were obtained of the FWM pump and sideband power as well as the statistics. It will be seen later that the statistical information obtained played a crucial role in confirming the physical interpretation of the experiments.

The 14-bit dynamic range of the camera system allows for weak FWM signals to be detected. A typical linear cross section of a FWM spectrum is shown on a linear scale [Fig. 4(a)] and logarithmic scale [Fig. 4(b)]. The spectrum is plotted first on a linear scale, which is comparable to the type of spectrum that would be obtained from a standard 8-bit video camera. The uniqueness of the GTRI CCD camera is shown in Fig. 4(b), where the spectrum is plotted on a logarithmic scale; the highest peaks in the spectrum are approximately four orders of magnitude above the noise. This spectrum shows many orders of sidebands, the highest orders just above the noise with a power less than 1% of the total pump power. The two central peaks are the pump waves at ω_1, higher frequency (blueshifted), and ω_2, lower frequency (redshifted). The first-order sidebands are located on either

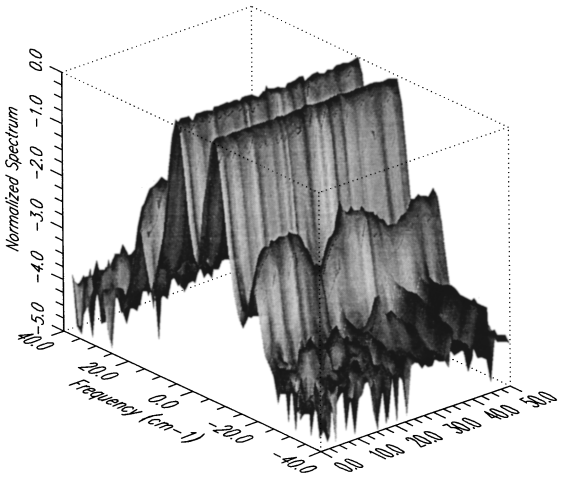

FIG. 5. Evolution of the FWM spectrum along the fiber from experiments for $P=2.1$ W and $\Omega=366$ GHz.

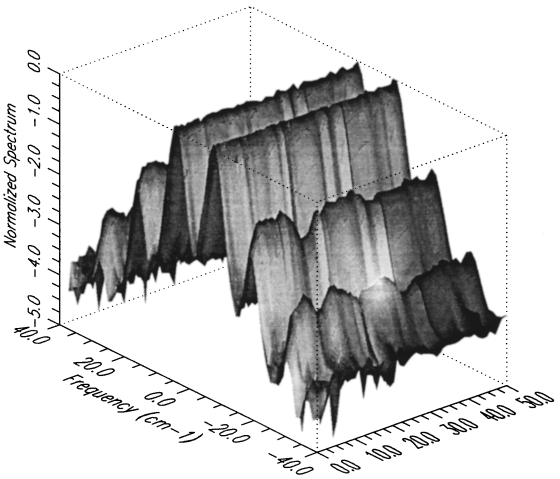

FIG. 6. Evolution of the FWM spectrum along the fiber from experiments for $P=5.5$ W and $\Omega=366$ GHz.

side of the pumps at $\omega_3=2\omega_1-\omega_2$ and $\omega_4=2\omega_2-\omega_1$. The detection of weak FWM sidebands at the fiber output presented here would not have been possible without the exceptional performance of this CCD camera system.

IV. EXPERIMENTS

The measurements of the dynamical evolution of four-wave-mixing processes along a length of single-mode polarization maintaining optical fiber were performed using two different values of the peak pump power: 2.1 and 5.5 W. The frequency separation between the pumps was held constant throughout the measurements at $\Omega=366$ GHz. The experiments began with 50.39 m of AT&T birefringent optical fiber [23]. Starting at this initial length, measurements of the FWM spectrum at the output of the fiber were made using the GTRI CCD camera. From these measurements, the conservation of total power and asymmetry [Eq. (4)] was tested for each data set. To check the conservation of these quantities, the total power and asymmetry in the single pumps propagating were calculated and compared with the power and asymmetry of the copropagating pumps. Data sets were accepted and kept if the conservation laws were preserved. In some cases, the presence of weak stimulated Raman scattering (SRS) was detected through the asymmetry relation. In the experiments tracing the evolution of the four-wave-mixing spectra along the fiber length no SRS was detected. After the initial measurements were made at the two input powers (2.1 and 5.5 W), 1–1.5 m of fiber was cut and cleaved. The fiber was cut and cleaved at the output side of the fiber to maintain approximately constant pump coupling to the fiber throughout the experiments. This process was repeated until the four-wave-mixing spectrum had been traced along the full 50.39 m of fiber for the two input power levels.

Figures 5 and 6 show three-dimensional plots of the average FWM output spectrum along the length of single-mode birefringent optical fiber. The vertical axis represents the intensity, normalized to the peak power in one of the pumps, plotted on a logarithmic scale. The pump frequencies are centered on $\pm\Omega/2$ and the fiber length is increasing into the page. In Fig. 5 the input power to the fiber is 2.1 W and first-order sidebands are clearly seen. Plotted on a logarithmic scale, the evolution of the power in the sidebands appears to evolve periodically with increasing fiber length. Figure 6 shows the evolution of the FWM spectrum for a pump input of 5.5 W. First-order sidebands are generated as well as ''weak'' second-order sidebands. The first-order sidebands appear to evolve periodically initially and, with increasing fiber length, evolve to a constant value.

A clearer picture of the evolution of the first-order sidebands is obtained by plotting the power in the sidebands as a function of length along the fiber. Figure 7 shows the evolution of the first-order sidebands as a function of length for a pump input of $P=2.1$ W. The two first-order sidebands are plotted separately: Fig. 7(a) shows the evolution of the blue sideband (blueshifted from the pumps) and Fig. 7(b) shows the red sideband (redshifted from the pumps). The solid line in the figure is generated by numerically solving the coupled amplitude equations truncated to six waves. The parameters

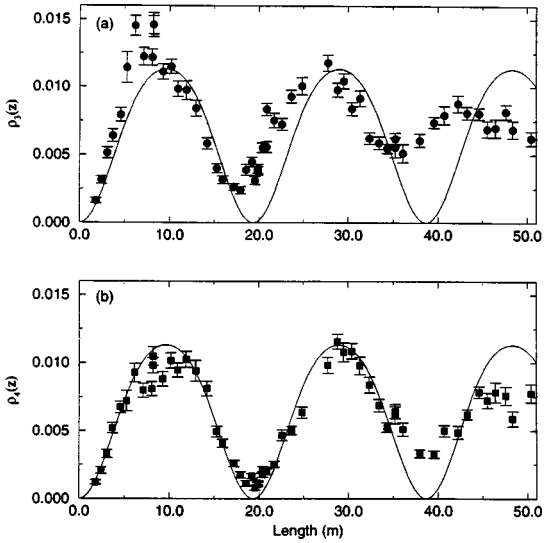

FIG. 7. Comparison between the experimental measurements (symbols) and the standard theoretical models (solid line) of the sideband evolution as a function of the fiber length for $P=2.1$ W and $\Omega=366$ GHz: dynamical evolution of the (a) blueshifted sideband and (b) redshifted sideband.

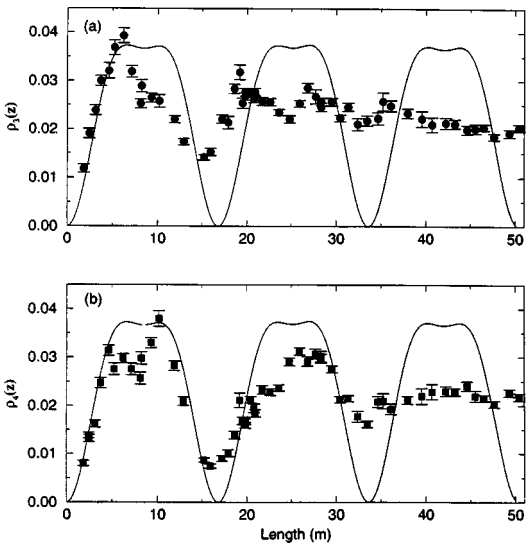

FIG. 8. Comparison between the experimental measurements (symbols) and the standard theoretical models (solid line) of the sideband evolution as a function of the fiber length for $P=5.5$ W and $\Omega=366$ GHz: dynamical evolution of the (a) blueshifted sideband and (b) redshifted sideband.

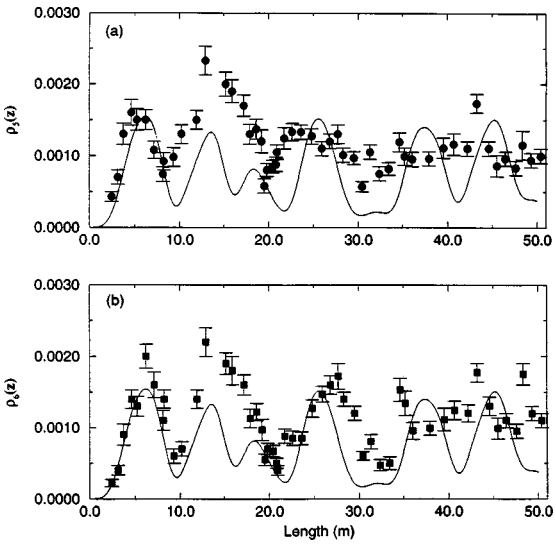

FIG. 9. Comparison between the experimental measurements (symbols) and the standard theoretical models (solid line) of the second-order sideband evolution as a function of the fiber length for $P=5.5$ W and $\Omega=366$ GHz: dynamical evolution of the (a) blueshifted sideband and (b) redshifted sideband.

$\beta^{(2)}$ and γ were determined by finding the best fit of the numerical simulations to the experimental data. The values obtained were $\beta^{(2)}=55\ \mathrm{ps}^2/\mathrm{km}$ and $\gamma=0.019\ \mathrm{m}^{-1}\ \mathrm{W}^{-1}$, both well within the regime expected for a central wavelength of 633 nm [1]. The measured sideband power, normalized to the total power in the fiber, is periodic with length, but it appears to be damping to a constant value. Also, the first minimum of the blue sideband trajectory occurs at a shorter distance than the first minimum for the red sideband. This contradicts the predictions of the coupled amplitude equations and the NLSE. The models predict essentially the same evolution for each sideband. The other difference between the two sidebands is the magnitude of the first maximum. The blue sideband has a larger maximum than the red sideband.

The apparent damping of the periodic sideband trajectory is seen more dramatically in Fig. 8, which shows the evolution of the first-order sideband power along the fiber for an input power of 5.5 W. Again the two first-order sidebands (blue and red) evolve with different trajectories. Furthermore, they also appear to damp to a constant value at a faster rate than for the case with a pump input power of 2.1 W. Both sets of experiments are compared with the numerical simulations in Figs. 7 and 8. The standard theoretical models do not account for either the damping of the sideband power or the different trajectories of the blue and red sidebands.

The FWM spectrum in Fig. 6 shows first-order sidebands as well as weak second-order sidebands for a pump input power of 5.5 W. Figure 9 shows the evolution of the power in the second-order sidebands with propagation length. The blueshifted and redshifted sidebands are plotted separately and the power is normalized to the total input power. The measured sideband power has a maximum of 0.2% of the total input. The 14-bit ADC used in the camera system limits the resolution to $1/16\,384=0.07\%$. Figure 9 shows a complex evolution of the sidebands. The sidebands are weak and just above the limits of resolution imposed by the detection system. A comparison is made using simulations based on the nonlinear Schrödinger equation. The NLSE is used in these simulations because it was found necessary to include higher-order sidebands (greater than second order) to model the dynamics.

A first set of experiments was performed using 20 m of the AT&T birefringent fiber. In these earlier measurements, the evolution of the sidebands was traced along the fiber using an input power of 2:1 W and a pump detuning of 366 GHz. A direct comparison between the sideband power along the length of 20 m of fiber with the sideband evolution along the 50.39 m of fiber was made. The two sets of data were found to yield the same results. Thus the observations of the damping of the sideband trajectory and the different evolutions of the individual sidebands are repeatable.

Another perspective on the evolution of the sidebands is gained through investigation of the sideband power dependence on the pump power [13]. Measurements were made of the sideband power as a function of pump power at a length of 50.39 m for two different values of the pump detuning. Figure 10 shows the power in the first-order sidebands as a function of input power using a pump detuning $\Omega=366$ GHz. The blue and red sidebands are plotted in Figs. 10(a) and 10(b), respectively. The input power was varied from approximately 2 to 15 W and the procedure outlined above was used for data collection. Pump depletion due to SRS was observed for pump powers greater than 10 W. For both the blue and red sidebands, the measurement peaks around 12 W and then begins to decrease with increasing pump power. This decrease can be attributed to significant pump depletion associated with Raman scattering. The solid lines in Fig. 10 were generated by numerically solving the coupled amplitude equations truncated to six waves using $\beta^{(2)}=55\ \mathrm{ps}^2/\mathrm{km}$ and $\gamma=0.019\ \mathrm{m}^{-1}\ \mathrm{W}^{-1}$. The numerical solutions yielded quite different dynamics from those observed experimentally.

The pump detuning was maintained at 366 GHz through-

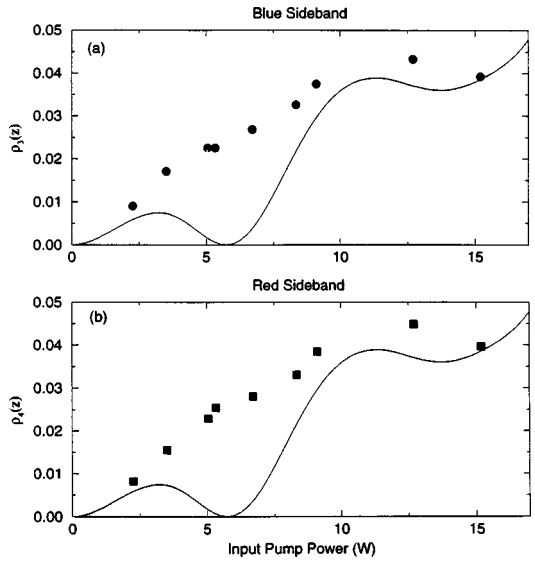

FIG. 10. Comparison between the experimental measurements (symbols) and the standard theoretical models (solid line) of the sideband power versus pump input power for $L=50.39$ m and $\Omega=366$ GHz: power in the (a) blueshifted sideband and (b) redshifted sideband.

out the experiments probing the evolution along the fiber length. Prior to cutting the fiber, a series of measurements of the sideband power dependence on the pump power were performed with a detuning twice as large: $\Omega=722$ GHz. Doubling the detuning resulted in a smaller conversion of power from the pumps to the sidebands. Figure 11 shows the results of these measurements. Only first-order sidebands were detected for the range of pump powers explored. Consequently, essentially periodic dynamics were predicted by the theoretical models. As in the 366-GHz detuning case, the sideband power steadily increased with pump power until stimulated Raman scattering began to deplete the pumps.

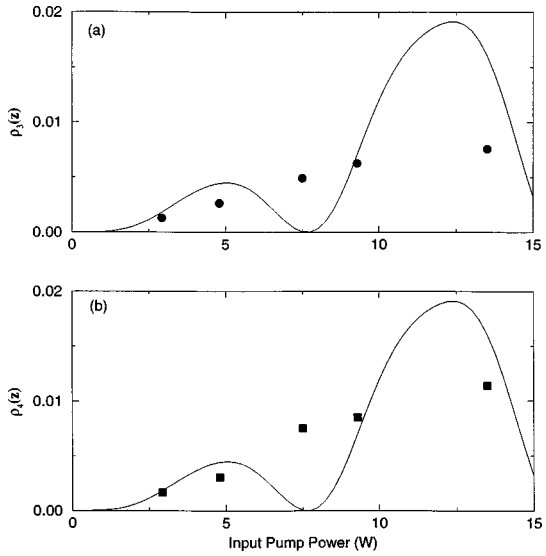

FIG. 11. Comparison between the experimental measurements (symbols) and the standard theoretical models (solid line) of the sideband power versus pump input power for $L=50.39$ m and $\Omega=722$ GHz: power in the (a) blueshifted sideband and (b) redshifted sideband.

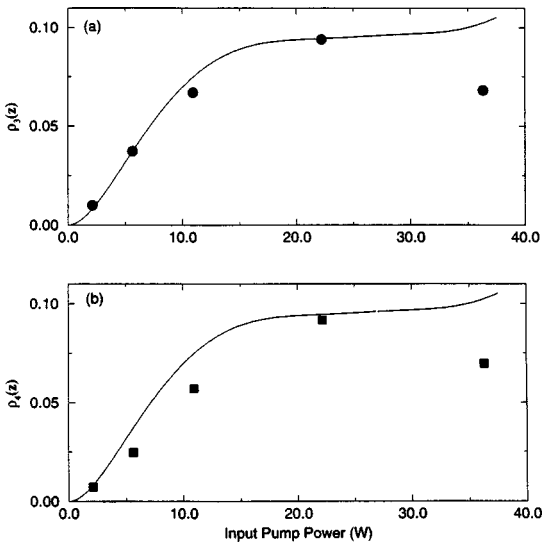

FIG. 12. Comparison between the experimental measurements (symbols) and the standard theoretical models (solid line) of the sideband power with pump input power for $L=5.52$ m and $\Omega=366$ GHz: power in the (a) blueshifted sideband and (b) redshifted sideband.

The numerical simulations again showed oscillations in the sideband power with increasing pump power, in marked contrast to the dynamics seen in the experiments.

To check some of the observed dynamics, a series of sideband power dependence measurements were performed at a length of 5.52 m with a detuning of 366 GHz. Figure 12 shows the sideband power as a function of input power. Raman scattering was observed for pump powers greater than 25 W. A comparison of the experimental measurements with numerical simulations shows very close agreement for pump powers less than 25 W. Thus, as the sidebands initially grow in the fiber, the numerical models can accurately predict the sideband dynamics. However, for longer fiber lengths the standard theory fails to predict the dynamical evolution of the pumps and sidebands as the pulses propagate through the fiber.

So far, only the dynamical evolution of the power in the sidebands has been discussed. It is also worth discussing the experimental FWM spectral envelope, which resembles a hyperbolic secant shape at the output of 50.39 m of fiber. The hyperbolic secant is a ubiquitous shape in nonlinear fiber optics and arises in the context of soliton propagation in fibers. Soliton propagation in the form of a hyperbolic secant pulse shape is found in the anomalous dispersion regime ($\beta^{(2)}<0$) [12,27]. However, the experiments in this research were performed in the normal dispersion regime. In the normal dispersion regime, dark-pulse solitons of the form of a hyperbolic tangent are predicted and have been observed [16].

Figure 13 shows some of the experimental FWM output spectra at a fiber length of 50.39 m, detuning $\Omega=366$ GHz, and with a range of input power levels (a) 2.1 W, (b) 5.5 W, (c) 8.3 W, and (d) 17.4 W. The solid line represents the experimental data and the dashed line is a curve fit to the spectral envelope. The curve is fit by $y(\omega)=A\ \mathrm{sech}(B\omega)$, where A and B are the fit parameters. The values used to generate the plots in Fig. 13 are (a) $A=3.85$

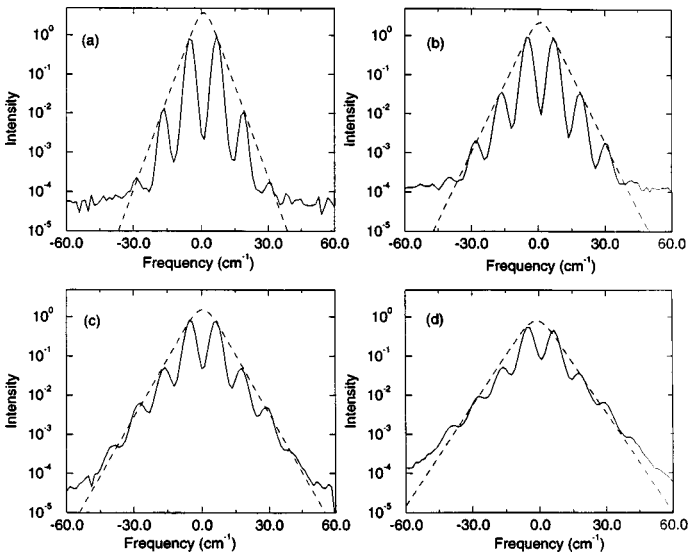

FIG. 13. Experimental FWM output spectrum (solid line) and hyperbolic secant envelope fit (dashed line) for pump input powers P of (a) 2.1 W, (b) 5.5 W, (c) 8.3 W, and (d) 17.4 W, fiber length $L=50.39$ m, and detuning $\Omega=366$ GHz.

and $B=0.36$, (b) $A=2.26$ and $B=0.27$, (c) $A=1.56$ and $B=0.23$, and (d) $A=0.81$ and $B=0.20$. Figure 13 shows close agreement between the hyperbolic secant shape and the experimental spectral envelope. For the lower input powers, the peaks in the spectra are distinct. However, as the input power increases, the peaks broaden and the spectrum begins to fill in.

In Fig. 13(d), with an input power of 17.4 W, the pumps are depleted by Raman scattering. Furthermore, close examination of the spectrum shows an asymmetry even though the initial conditions on the pump waves were symmetric, i.e., $\rho_1(0)=\rho_2(0)$. As the waves copropagate in the fiber, photons from the band of frequencies generated through four-wave mixing will be downshifted by spontaneous and stimulated Raman scattering. The Raman gain spectrum ranges from zero to tens of terahertz frequency shift from the pumps. For silica glass, the maximum Raman gain occurs at a downshifted frequency of 13.2 THz (several orders of magnitude larger than the pump detuning) [1]. However, the Raman gain is nonzero near a zero-frequency shift. Thus, in Fig. 13(d) the observed asymmetry in the spectrum arises from strong stimulated Raman scattering.

These experiments exposed several discrepancies in the comparison of experiment and theory and illustrated the inadequacy of the standard theoretical models to predict the observed dynamics over the full length of fiber investigated. The next section will present modifications to the theoretical models to allow a quantitative comparison of experimental observations and numerical simulations. The key aspects of the experiments to be addressed are the damping of the periodic sideband trajectories with length and the difference between the red and blue sideband trajectories.

V. THEORY VERSUS EXPERIMENT

This section develops a theoretical description that includes two effects that had not previously been considered. We consider the effect of a multimode pump laser at the fiber input and investigate the resulting dynamical evolution of the sidebands. By modeling one of the pump lasers as two closely spaced longitudinal modes, the subsequent dynamical evolution of the sidebands is altered dramatically. By introducing this asymmetry in the mode structure of the pump input, the resultant dynamics for the blue and red sidebands begin to approach the sideband dynamics observed in the experiments. However, the damping of the periodic trajectories seen in the experiments is still not explained with the simple multimode structure at the input. Building on the multimode analysis, one then introduces weak phase fluctuations to the pump waves propagating along the fiber. The combination of both the multimode pump input and weak phase perturbations along the fiber is found necessary to accurately predict the experimental observations. Excellent agreement is thus finally obtained on comparing predictions based on the stochastic multimode model with experiments.

A. Multimode pump input

As mentioned previously, the dye laser systems used in the experiments were designed for narrow-band operation. However, the resolution of our instrumentation limits the ability to measure the linewidth of the lasers and distinguish single versus multiple mode operation. Thus either of the dye laser outputs may have consisted of several longitudinal modes. We examine the impact of multimode operation on the dynamical evolution of the sidebands by introducing a multimode pump input to the theoretical models. The sideband evolution predicted from numerical solutions of both the NLSE and the coupled amplitude equations with a multimode input is found to exhibit similar dynamics when compared with the experimental observations.

To model wave propagation in the fiber using a multimode pump input, both the nonlinear Schrödinger equation and the coupled amplitude equations discussed earlier can be used. The NLSE requires only a modification of the input pulses. The input spectrum can be set for one, two, three, etc., modes in each pump laser. Thus a variety of initial pump conditions can be investigated. Starting with the simplest case, Fig. 14 shows an example of (a) the Gaussian input pulse and (b) corresponding spectrum to the NLSE, with two modes in the blueshifted pump and one mode in the redshifted pump. In Fig. 14(b) the spectrum is plotted with the pump detuning normalized to unity and the pumps centered about the zero-frequency shift. The input is a Gaussian pulse modulated by the pump detuning and the longitudinal mode spacing. The longitudinal mode spacing ($\Delta\nu$) were chosen to be 0.5 GHz, which is consistent with the expected spacing from the experiments, and the pump detuning is 366 GHz. The initial conditions on the pumps were chosen so that the conservation relation for the asymmetry [Eq. (4)] is zero, i.e., $\rho_1=\rho_2$. Figure 15 shows the FWM output spectrum generated from the multimode input. The sidebands and pumps now consist of many frequencies. To estimate the relative power in the pumps and sidebands, the power in the band of frequencies centered around the primary frequency is summed and then normalized to the total power in the spectrum; for example, the blue pump power ρ_1 is calculated from summing the power in the frequency components located between zero and one. For consistency, the same notation used throughout this paper is retained to represent the

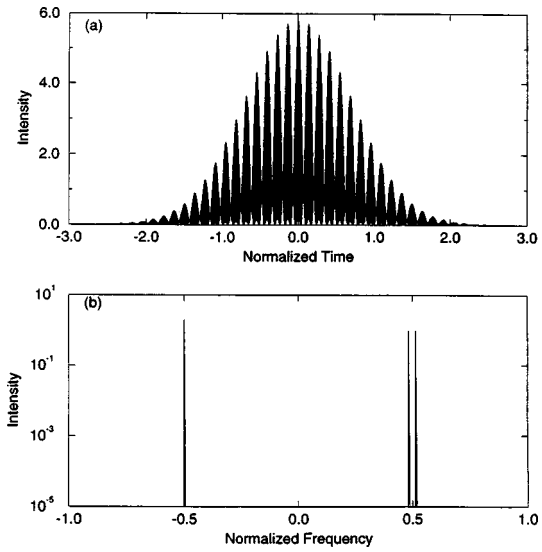

FIG. 14. Multimode pulse input to the NLSE: (a) input pulse in the time domain and (b) input spectrum.

power in the pumps and sidebands, e.g., ρ_3 represents the relative power in the blue first-order sideband even though now it consists of multiple frequency components.

The split step Fourier method is used to propagate the pulses along the fiber [1]. Figure 15 shows a schematic representation of the FWM output spectrum after propagation through a length of fiber with the multimode input. The evolution of the four-wave-mixing processes is now more complex: Not only is there mixing between the distantly spaced pump frequencies but there is mixing between the closely spaced longitudinal modes. A difficulty of using the NLSE to model the multimode input is the size of the FFT that must be computed. Since the longitudinal mode spacing is several orders of magnitude smaller than the pump detuning, the number of points necessary to represent the pulse spectrum is large, greater than or equal to 2^{15}. The computation algorithm sets limits on the number of points used to represent the spectrum and the spectrum will necessarily be truncated. In general, the NLSE with single-mode inputs yields the ability to work with a broad spectrum consisting of many orders of sidebands, a definite advantage over the coupled amplitude equations.

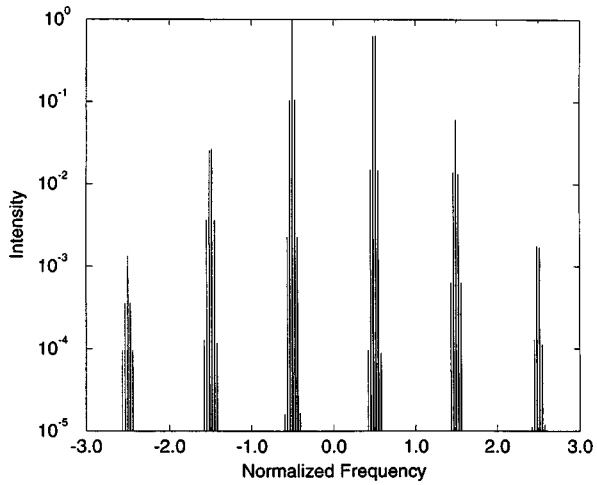

FIG. 15. Multimode output spectrum from the NLSE after propagation through several meters.

Extending the modeling of the multimode input to the coupled amplitude equations, the general form of the equations given in Eq. (3) is used to generate a new set of coupled amplitude equations. The frequencies in these equations now include the longitudinal mode spacing. Thus the wave-vector mismatch will now be proportional to $(\Omega \pm \Delta\nu/2)^2$, $(\Omega \pm 3\Delta\nu/2)^2$, etc., whereas in the single-mode model, the mismatch was proportional to Ω^2. The number of frequency components necessary to model the FWM dynamics, including up to second-order sidebands, results in at least 100 terms in each equation. Using Eq. (3), a *C* program was written to find the allowed combinations of k, m, and n. The multimode four-waving-mixing equations were then stored to a file in a subroutine format to be called from the integration programs.

For simplicity, the case of two longitudinal modes in the blue pump and one in the red pump is considered. The blue pump was initially chosen to be multimode because the fluctuations in experimental measurements of the linewidth were larger than those in the red pump. The single-mode input standard model consists of six complex coupled field equations and includes the pumps, first-order sidebands, and second-order sidebands. Terms up to second-order sidebands were included since they were observed in the experiments for a pump input of 5.5 W. With the multimode model, including up to second order in the sideband frequencies, it was found necessary to include at least 29 complex field equations. The corresponding number of frequency components in each of the six frequency bands is as follows: blue pump, 6; red pump, 5; blue first-order sideband, 5; red first-order sideband, 6; blue second-order sideband, 4; and red second-order sideband, 3 (see Fig. 15). This minimum number of equations was determined by a comparison with solutions of the NLSE using a multimode pump input with $P = 5.5$ W, $\Omega = 366$ GHz, $\beta^{(2)} = 55$ ps^2/km, and $\gamma = 0.019$ W^{-1} m^{-1}. Thus the coupled amplitude equations even with the simplest multimode input case become quite cumbersome rapidly. However, the advantage of using the coupled amplitude equations when including stochastic processes will be discussed.

Figure 16 shows the sideband evolution generated from solution of the coupled amplitude equations with a multimode input (dual-mode blue pump and single-mode red pump) with $\Omega = 366$ GHz, $\Delta\nu = 0.5$ GHz, and a pump input of 2.1 W. The blue and red sidebands are plotted separately. The experimental data presented previously are plotted along with the simulations for comparison. Modification of the blue pump from the single mode to the dual mode alters the sideband evolution dramatically. As a comparison, for an input power of 2.1 W, the single-mode model predicts a sideband trajectory that is a sinusoid with no distinction between the red and blue first-order sidebands [28]. The multimode model, however, yields two very distinct trajectories for the blue (ρ_3) and red (ρ_4) sidebands. The difference in the sideband trajectories arises from the asymmetry imposed in the input. If the pumps were both modeled as dual mode the sinusoid evolution seen with single-mode input would be recovered.

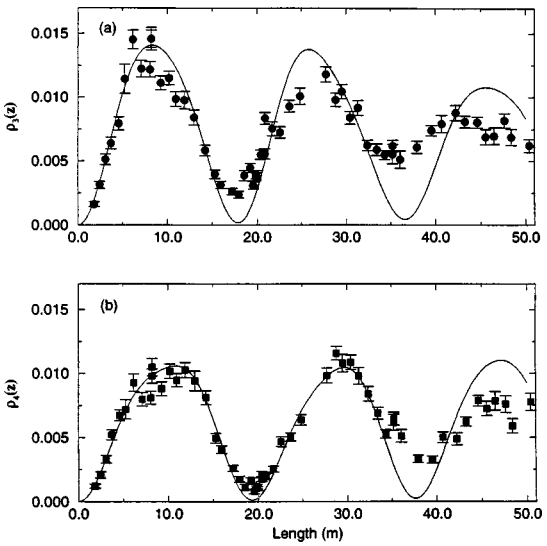

FIG. 16. Comparison between the experimental measurements (symbols) and the multimode model (solid line) of the sideband evolution as a function of fiber length for $P=2.1$ W, $\Omega=366$ GHz, $\Delta\nu=0.5$ GHz, $\gamma=0.019\ \mathrm{W}^{-1}\,\mathrm{m}^{-1}$, and $\beta^{(2)}=55\ \mathrm{ps}^2/\mathrm{km}$: dynamical evolution of the (a) blueshifted sideband and (b) redshifted sideband.

Figure 17 shows the dynamical evolution of the sideband power for a pump input of 5.5 W, using the dual-mode blue pump input. Again, the experimental data are plotted for comparison. The coupled amplitude equations are truncated to 29 complex field equations. The dynamics exhibited by the blue and red sidebands with this model are significantly different. Within the first 10 m, the model follows the evolution quite well and yet the damping observed in the experimental measurements with increasing length makes a comparison difficult. Overall, the multimode model yields promising results for predicting the dynamical evolution of

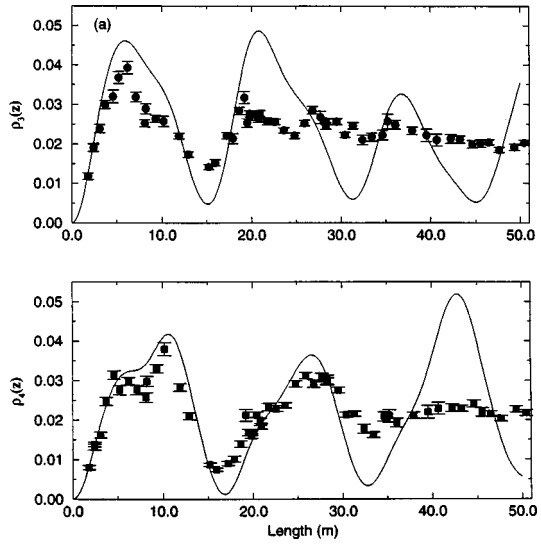

FIG. 17. Comparison between the experimental measurements (symbols) and the multimode model (solid line) of the sideband evolution as a function of fiber length for $P=5.5$ W, $\Omega=366$ GHz, $\Delta\nu=0.5$ GHz, $\gamma=0.019\ \mathrm{W}^{-1}\,\mathrm{m}^{-1}$, and $\beta^{(2)}=55\ \mathrm{ps}^2/\mathrm{km}$: dynamical evolution of the (a) blueshifted sideband and (b) redshifted sideband.

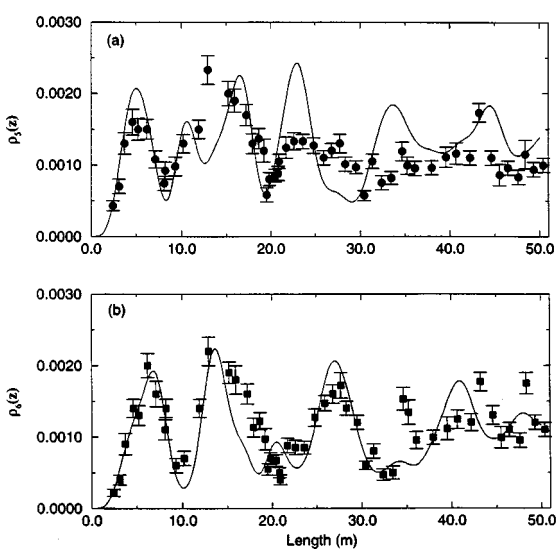

FIG. 18. Comparison between the experimental measurements (symbols) and the multimode model (solid line) of the second-order sideband evolution as a function of fiber length for $P=5.5$ W, $\Omega=366$ GHz, $\Delta\nu=0.5$ GHz, $\gamma=0.019\ \mathrm{W}^{-1}\,\mathrm{m}^{-1}$, and $\beta^{(2)}=55\ \mathrm{ps}^2/\mathrm{km}$: dynamical evolution of the (a) blueshifted sideband and (b) redshifted sideband.

the sidebands. The modeling of the damping of the sideband trajectories will be discussed in Sec. V B.

As another comparison of the multimode input model with experiment, Fig. 18 shows the evolution of the second-order sidebands with propagation distance. Terms including up to at least third-order sidebands must be included in the model to properly predict the dynamics of the second-order sidebands. The coupled amplitude equations including only up to second order were found to be inadequate. Thus the nonlinear Schrödinger equation was used to easily include higher-order sidebands. A comparison of the second-order sideband and predictions based on the NLSE with a multimode input shows close agreement. The second-order sidebands are weak and yet for fiber lengths less than 20 m the simulations follow the experimental measurements closely. However, beyond 20 m the blue second-order sideband [Fig. 18(a)] appears to be damping to a constant value.

As mentioned earlier, the model can be extended to include various combinations of pump inputs, for example, three modes in one of the pumps and two or one in the other pump. No significant difference was found in the first-order sideband evolution for the different combinations of asymmetric multimode input, for the parameter regimes investigated; $L_{\max}=50.4$ m, $P<6$ W, $\Omega=366$ GHz, and $\Delta\nu=0.5$ GHz. As the fiber length increases beyond 50.4 m, differences in the trajectories arise between the various asymmetric combinations for the input. Referring to Fig. 15, the spectrum broadens around the central frequency components due to FWM between the longitudinal modes. The longitudinal mode spacing used in these simulations is small compared to the pump detuning. Furthermore, since the mode spacing is small, the FWM processes between adjacent modes will evolve with a period much longer than the fiber lengths considered in this research. Subtle differences in the sideband evolution will arise for different mode structures as the fiber length increases due to the different dynamics be-

tween adjacent modes. Only the simplest case of multimode input was considered for comparison with these experiments.

B. Stochastic phase fluctuations

The previous theoretical analyses presented have been limited to deterministic models. We now turn to modeling of stochastic processes along the fiber length as well as including stochastic initial conditions on the pump inputs. The latter are included in the modeling to closely imitate the conditions present in the experiments. The former examines the impact on the dynamical evolution of the four-wave-mixing processes when weak fluctuations are added to the phase of each of the waves copropagating along the fiber. These phase fluctuations are found to damp the sideband periodic trajectories to a constant value. A comparison with the experimental observations is made and excellent agreement is found.

Consider a physical process that acts to perturb the phase of the waves propagating along the fiber. The physics of this phase noise could arise from a number of sources such as fiber medium inhomogeneities [29,30], Brillouin scattering, or Raman scattering [1]. In the experiments, there was no indication that these sources were present. However, the existence of these processes could have been lost in the background noise of the instrumentation. Identification of the physical process generating the noise through both experiments and modeling is a promising area for future research. A strong candidate for the source of phase noise is stimulated Raman scattering that builds up from a spontaneous noise background. Recalling the experiments probing the sideband power dependence on the pump input power, for a 50 m length of fiber significant Raman scattering was detected for pump inputs greater than 10 W. Thus it is highly likely that very weak (less than four orders of magnitude down from the pumps) Raman scattering was present in the measurements.

There are two theoretical models that may serve as the core set of equations to model the nonlinear wave propagation along with stochastic processes in the fiber. The multimode coupled amplitude equations, developed previously, were used for the stochastic modeling in this research. A model incorporating the phase noise into the nonlinear Schrödinger equation is desirable as well. However, algorithms to properly include the necessary stochastic terms in the NLSE are not available at this time. Thus the remainder of the research will use the coupled amplitude equations. Integration of the amplitude equations proceeded as follows. After the initial conditions on the input were set, the multiple waves were propagated in the fiber using a fourth-order Runge-Kutta integration [21] with a step size Δz (typically 10^{-3} m). After each integration step, the complex field amplitudes were converted to intensity and phase. The phase ϕ_j of each wave at frequency ω_j was modified according to

$$\phi_j(z+\Delta z)=\phi_j(z)+\delta\phi_j, \tag{5}$$

where the phase fluctuations are represented by $\delta\phi_j$. The intensity and phase were then converted back to the complex field amplitudes. The field was then propagated another step Δz and the process was repeated for each integration step.

Since the exact source generating the noise is not known, the phase fluctuations are taken to be δ correlated along the fiber and are considered to be independent sources for each wave. The Box-Muller algorithm was used to generate Gaussian deviates from computer-generated uniform deviates [21,31]. The fluctuations are given by

$$\delta\phi_j=\sqrt{-2\sigma_{\phi_j}\Delta z\ \ln(r_1)}\cos(2\pi r_2) \tag{6}$$

and

$$\delta\phi_{j+1}=\sqrt{-2\sigma_{\phi_{j+1}}\Delta z\ \ln(r_1)}\sin(2\pi r_2), \tag{7}$$

where r_1 and r_2 are uniformly distributed random numbers on the interval [0,1] and σ_{ϕ_j} is the standard deviation of the phase fluctuations for a given frequency component. For simplicity in the numerical computations, the phase fluctuations were added to only the frequency components associated with the two pump waves. However, computations were also performed adding phase noise to all components; there was no detectable difference in the resulting sideband dynamics for the parameters investigated. This is reasonable in the regime of primary interest since for pump powers less than 6 W the pump intensities are much larger than the sidebands and thus make the strongest contribution to the FWM dynamics. Typically, the noise strengths σ_j were chosen to be of the same order of magnitude for each pump.

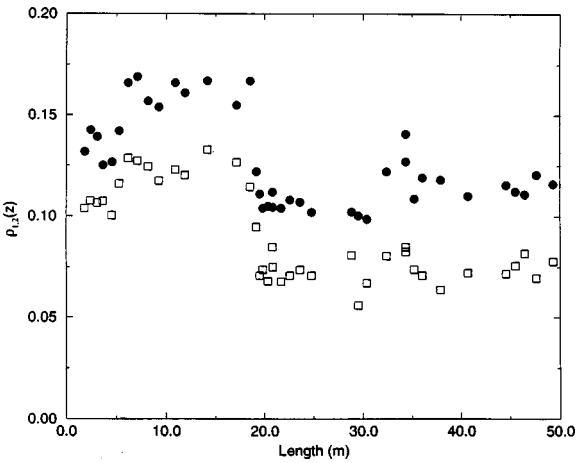

FIG. 19. Measured input pump power standard deviation as a function of fiber length: blueshifted pump (closed circles) and redshifted pump (open squares).

C. Stochastic initial conditions

Previous studies showed that fluctuations in the initial conditions of the pumps could have a significant impact on the dynamics of the FWM processes in the fiber [13,18]. To model the initial conditions of the experiments, measurements of the pump fluctuations were included in the input to the integration of the equations. To measure the pump fluctuations, each pump was propagated alone in the fiber for each fiber length and pump power. The mean intensity, normalized to unity, and standard deviation were calculated from the output spectra. The intensity in the pumps was found to be Gaussian distributed. Figure 19 shows the measured standard deviation in the normalized pump power as a function of length along the fiber. The blue and red pump standard deviations are plotted separately. The blue laser has

a higher mean intensity fluctuation than the red, which is probably associated with multiple longitudinal modes in the blue pump. The experimental measurements over the full length of optical fiber were performed over a long period of time (approximately 1 yr). As can be seen from Fig. 19, the pump intensity standard deviation varied with time.

The numerical simulations were performed with fluctuations in the input pump intensity as well as fluctuations in the detuning. The measured frequency fluctuations had a magnitude of less than 1 GHz, several orders of magnitude smaller than the pump detuning of 366 GHz. Including the frequency fluctuations in the simulations was found to have no measurable impact on the resulting dynamical evolution of the sidebands. However, the pump power fluctuations were large ($\sim 10\%$) and could not be neglected. The pump input was of the form

$$U_j(0) = \sqrt{\rho_j(0)}\, e^{i2\pi r_j}, \tag{8}$$

where ρ_j is the intensity and r_j is a uniformly distributed random number in the interval [0,1], which selects a nonzero initial phase. For completeness r_j is included here. However, randomizing the initial phase had no measurable impact on the resulting evolution of the power in the waves. The pump intensity input to Eq. (8) for each component in the dual-mode pump was set according to

$$\rho_{1k}(0) = \tfrac{1}{2}\rho + \tfrac{1}{2}\delta\rho_1, \tag{9}$$

where k represents each mode, and for the single-mode pump

$$\rho_2(0) = \rho_{\text{ave}} + \delta\rho_2, \tag{10}$$

where ρ_{ave} is typically set to unity for both pumps and $\delta\rho$ are the fluctuations in the pumps and are generated using the Box-Muller algorithm [21]. The fluctuations are generated using the measured values of the standard deviation in the pump intensities (see Fig. 19) and are given for the blue pump, by

$$\delta\rho_1 = \sqrt{-2\sigma_{\rho_1}^2 \ln(r_1)}\cos(2\pi r_2) \tag{11}$$

and, for the red pump,

$$\delta\rho_2 = \sqrt{-2\sigma_{\rho_2}^2 \ln(r_1)}\sin(2\pi r_2). \tag{12}$$

Computations with the multimode model (for the dual-mode pump) used the same noise strength for each longitudinal mode. The following subsection will discuss the specific values used in the numerical simulations and compare with the experiments.

D. Numerical simulations

The numerical simulations were performed using the multimode coupled amplitude equation along with the stochastic conditions discussed above. A complication arose when adding the phase fluctuations to the waves, which resulted in a ''noise-induced'' drift [32]. This is a feature of multiplicative noise sources in which the noise added causes the sidebands to grow with propagation. Even though the noise is additive to the phase, the equations are cubic in the complex field and thus the phase noise is multiplicative when coupled back into the field equations. Including phase noise in the FWM calculations resulted in trajectories for the sideband power with length, which were damped periodic trajectories with an increasing slope. To remove this artifact of the computations, a linear loss term $-\alpha U_j$ was added to each of the complex field equations. The loss coefficient α was then set by finding the value that removed this increasing slope. In theory, the mathematical form of α can be derived from the equations and is a function of the noise strength [32]. However, the size of the system of coupled propagation equations made the technique for estimation intractable, even for the simplest approximate form of the equations.

The strength of the phase noise used in all of the following simulations was determined by fitting the simulations to the experimental data. The values found to give the best fits were $\sigma_{\phi_1} = 0.0067\ \text{m}^{-1}$, $\sigma_{\phi_2} = 0.005\ \text{m}^{-1}$, and $\alpha = 0.0046\ \text{m}^{-1}$. For comparison with the experiments tracing the evolution of the sidebands along the fiber, the simulations were the result of two calculations, one from 0 to 20 m and the other from 0 to 50.4 m. The calculation from 0 to 20 m replaces the first 20 m of the 0–50.4 m simulations. This was necessary since the initial conditions on the pump fluctuations were larger (due to the laser adjustments for the measurements, which took several months) for lengths less than 20 m (see Fig. 19). The fluctuations in the pump intensities were set at $\sigma_{\rho_1} = 0.20$ (blue) and $\sigma_{\rho_2} = 0.11$ (red) to generate the curves from 0 to 20 m and $\sigma_{\rho_1} = 0.12$ and $\sigma_{\rho_2} = 0.05$ to generate the curves from 20 to 50.4 m. The other parameters were set at $\beta^{(2)} = 55\ \text{ps}^2/\text{km}$, $\gamma = 0.019\ \text{W}^{-1}\,\text{m}^{-1}$, $\Omega = 366$ GHz, and $\delta\nu = 0.5$ GHz. The numerical simulations compute both an average and standard deviation from 50 trajectories. Simulations were done for 100 trajectories and it was determined that accurate statistics the (standard deviation was less than 5%) were obtained for as few as 50 trajectories. Thus, to reduce computation time the statistics are calculated from 50 runs.

Figures 20(a) and 21(a) show the blue and red sideband trajectories, respectively, for an input power of 2.1 W. The experimental data are plotted with the numerical solution of the multimode coupled amplitude equations including both phase noise at each integration step and fluctuating the pump inputs. The multimode model with the inclusion of stochastic initial conditions and, most importantly, phase fluctuations along the fiber length, results in predictions that are very close to the experimental observations of the dynamical evolution of the sidebands. Figures 20(b) and 21(b) show the measured standard deviation in the sideband power along the fiber length for the blue and red sidebands, respectively. The standard deviation was also calculated from the numerical simulations. Excellent agreement is found between the model and experimental measurements. Throughout the course of this research, many stochastic models have been investigated and this model is the only one found that reproduces the evolution of both the average power and fluctuations in the sidebands.

For an input power of 5.5 W, Figs. 22 and 23 show a comparison between the numerical simulations and experimental data for the blue and red sidebands, respectively. The red sideband trajectories in Fig. 23 show excellent agreement

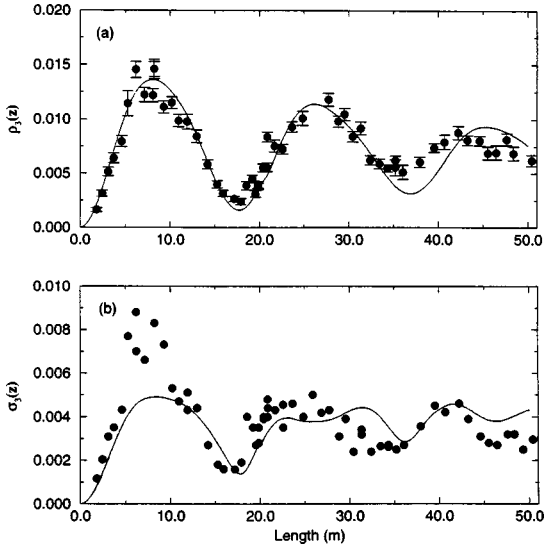

FIG. 20. Comparison between the experimental measurements (symbols) and the stochastic multimode model (solid line) of the blue sideband evolution as a function of fiber length for $P=2.1$ W, $\Omega=366$ GHz, $\Delta\nu=0.5$ GHz, $\gamma=0.019\ \mathrm{W}^{-1}\,\mathrm{m}^{-1}$, and $\beta^{(2)}=55\ \mathrm{ps}^2/\mathrm{km}$: dynamical evolution of the (a) power in the blue-shifted sideband and (b) measured fluctuations.

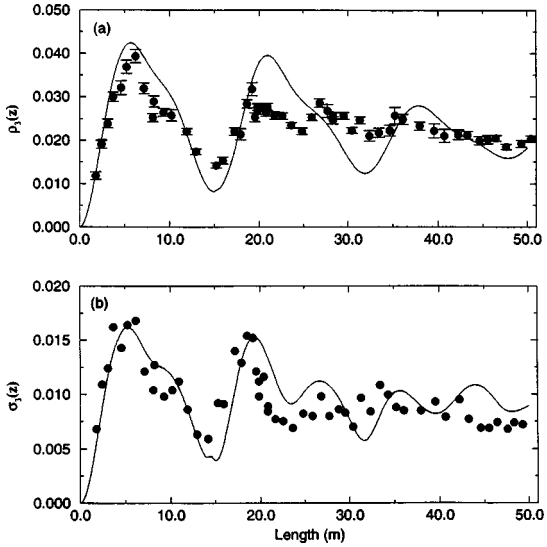

FIG. 22. Comparison between the experimental measurements (symbols) and the stochastic multimode model (solid line) of the blue sideband evolution as a function of fiber length for $P=5.5$ W, $\Omega=366$ GHz, $\Delta\nu=0.5$ GHz, $\gamma=0.019\ \mathrm{W}^{-1}\,\mathrm{m}^{-1}$, and $\beta^{(2)}=55\ \mathrm{ps}^2/\mathrm{km}$: dynamical evolution of the (a) power in the blue-shifted sideband and (b) measured fluctuations.

between the numerical model and experiment. The power in the red sideband from numerical solutions is periodic and appears to be at the appropriate rate. However, the blue sideband power trajectory shown in Fig. 22(a) does not reproduce the experimental measurements as closely. The numerical simulations at this pump power result in a blue sideband power evolution that does not damp as quickly as the experimental observations. However, the fluctuations measured in the experiments are fairly well predicted by the numerical simulations as shown in Figs. 22(b) and 23(b) for both the blue and red sidebands, respectively. The discrepancy in the damping seen between the experiment and model of the blue sideband power evolution could arise from several effects. The strength of the phase noise was the same for both the 2- and 5.5-W calculations. Many simulations have been performed to optimize the values used for the phase noise strengths. The values used in these simulations were optimized in the sense they gave the best fit to the experimental data. A better approach would be to identify the physical phenomena generating the phase fluctuations and with this knowledge the magnitudes of σ_{ϕ_1} and σ_{ϕ_2} could be esti-

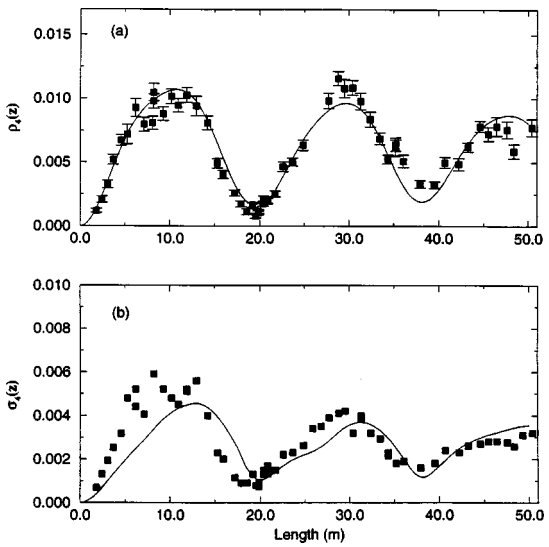

FIG. 21. Comparison between the experimental measurements (symbols) and the stochastic multimode model (solid line) of the red sideband evolution as a function of fiber length for $P=2.1$ W, $\Omega=366$ GHz, $\Delta\nu=0.5$ GHz, $\gamma=0.019\ \mathrm{W}^{-1}\,\mathrm{m}^{-1}$, and $\beta^{(2)}=55\ \mathrm{ps}^2/\mathrm{km}$: dynamical evolution of the (a) power in the redshifted sideband and (b) measured fluctuations.

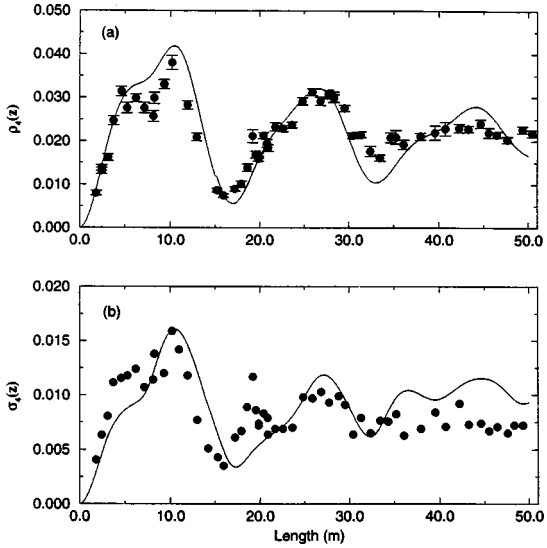

FIG. 23. Comparison between the experimental measurements (symbols) and the stochastic multimode model (solid line) of the red sideband evolution as a function of fiber length for $P=5.5$ W, $\Omega=366$ GHz, $\Delta\nu=0.5$ GHz, $\gamma=0.019\ \mathrm{W}^{-1}\,\mathrm{m}^{-1}$, and $\beta^{(2)}=55\ \mathrm{ps}^2/\mathrm{km}$: dynamical evolution of the (a) power in the redshifted sideband and (b) measured fluctuations.

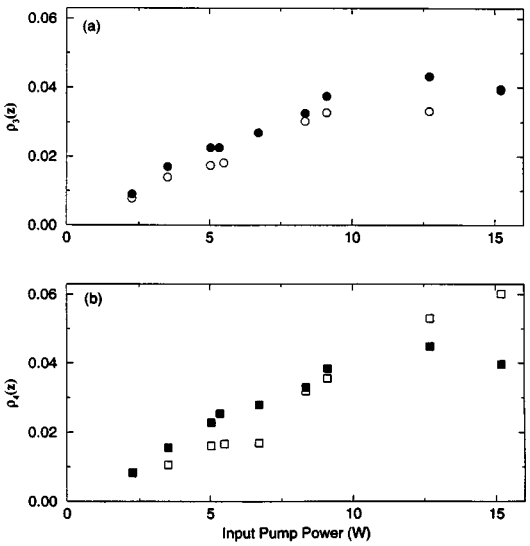

FIG. 24. Comparison between the experimental measurements (closed symbols) and the stochastic multimode model (open symbols) of the sideband power versus pump input power for $L = 50.39$ m, and $\Omega = 366$ GHz: power in the (a) blueshifted sideband and (b) redshifted sideband.

mated from the physics. Another benefit of identifying the physics of the phase noise is that the noise could be properly included in a model based on the nonlinear Schrödinger equation.

As a confirmation of the multimode model with phase noise, numerical simulations were performed examining the sideband power dependence on the input power at a length of 50.4 m. Figures 24 and 25 show the power in the sidebands as a function of input power for a pump detuning of 366 and 722 GHz, respectively. The experimental measurements of the sideband powers are represented by closed circles in Figs. 24(a) and 25(a) (blue sideband) and closed squares in Figs. 24(b) and 25(b) (red sideband). The results of numerical simulations are represented by open circles in Figs. 24(a) and 25(a) and open squares in Figs. 24(b) and 25(b). The numerical simulations follow the general trend seen in the experiments. A large deviation occurs for pump powers greater than 10 W where the pumps begin to be depleted by stimulated Raman scattering. Below 10 W the experimental measurements of the red sidebands tend to be higher than the simulations; this increase arises from weak scattering of the blue photons to the red. With the smaller detuning (366 GHz), care must be taken to account for all orders of sidebands and for powers greater than 6 W probably third- and fourth-order sidebands are generated. However, with this model, including only up to second-order sidebands yields predictions in close agreement with experimental measurements especially when compared with the predictions based on the deterministic single-mode input coupled amplitude equations.

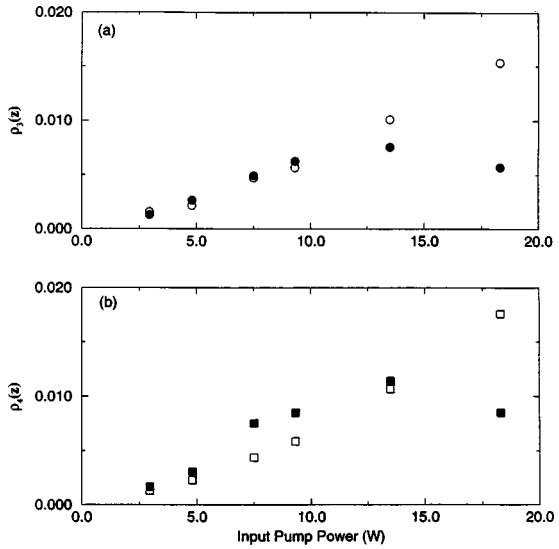

FIG. 25. Comparison between the experimental measurements (closed symbols) and the stochastic multimode model (open symbols) of the sideband power versus pump input power for $L = 50.39$ m and $\Omega = 722$ GHz: power in the (a) blueshifted sideband and (b) redshifted sideband.

We have presented an approach to modeling the dynamical evolution of four-wave-mixing processes along an optical fiber. This modeling was motivated by the standard theoretical models inability to predict the results of experimental measurements presented in Sec. III. The two critical features of the model were a multimode pump input along with phase fluctuations added along the fiber length. The multimode pump input was found to alter the resulting sideband dynamics significantly. Due to an asymmetry introduced in the input, the blue and red sidebands evolved with different trajectories along the fiber. Furthermore, by adding weak phase fluctuations to the copropagating waves, the periodic sideband trajectories were found to damp out. Figures 20–25 show comparisons between the experimental measurements of the sideband dynamics and the stochastic multimode model. The experimental observations brought to light several questions regarding the dynamics of the four-wave-mixing processes in the fiber.

VI. CONCLUSIONS

The dynamical evolution of four-wave-mixing processes in an optical fiber has been investigated. This research consisted of experimental, theoretical, and numerical computations. The focus of this work was to experimentally trace the evolution of the sidebands, generated through FWM, along a length of optical fiber. Previous theoretical work suggested that, in certain parameter regimes, the sidebands exchange energy with the pumps periodically [13,14]. Specifically, in the undepleted pump regime [28], the sideband power evolves as a sinusoid with fiber length. Previous experiments had probed the dynamics for short fiber lengths (less than 2 m) [13]; however, the periodic evolution had never been directly verified.

The FWM spectral evolution along 50 m of fiber for two input pump power regimes was investigated. The experimental work consisted of measuring the FWM spectrum output from an optical fiber at different lengths in the fiber. Specifically, a low-noise, high-resolution CCD camera made at Georgia Tech Research Institute was used [26] to detect weak (less than 1% of the power in the pumps) sidebands. With this resolution, measurements of the power in the first-order sidebands for input pump powers (2.1 and 5.5 W) were made using a pump detuning of 366 GHz. In the case of a

pump input of 2.1 W, the sideband power evolution is expected to follow a sinusoid along the length of the fiber. Experiments showed that the power in the sideband evolved periodically, but that the evolution followed a damped sinusoid. The experiments also found that the two first-order sidebands (blue-shifted and redshifted from the two pumps) had different evolutions along the fiber. Neither the damping nor the different evolutions were predicted by theory. Using a pump input power of 5.5 W, the evolution of both first- and second-order sidebands was also measured. For a pump input of 5.5 W which the damping in the first-order sidebands appeared to occur faster than in the 2.1-W case.

Experiments probing the dependence of the sideband power on the input power for two different values of the detuning (366 and 722 GHz) were also performed at the output of 50 m of fiber. With a detuning of 366 GHz, the sideband power for pump inputs ranging from 2 to 17 W which was measured. A comparison of theoretical predictions with the measurements showed a large discrepancy both quantitatively and qualitatively. The measurements of the sideband power as a function of pump input power with 722-GHz detuning showed the same discrepancies with the theoretical models as the 366-GHz detuning case. Another set of measurements were performed at a length of 5 m with a pump detuning of 366 GHz. Comparisons of the measured sideband powers with theoretical predictions, for this case, showed excellent agreement up to a pump input power of 25 W. For higher powers, the deviation between experiment and theory was due to other competing processes (stimulated Raman scattering) not accounted for in the theoretical model. The results of the measurements show that the initial evolution of the FWM spectrum in the fiber is modeled well by the standard theory. However, beyond the initial growth of the spectrum the models do not predict, even qualitatively, the experimental observations.

Three-dimensional plots of the evolution of the four-wave-mixing spectrum in the fiber indicate that the spectrum was evolving to a stable profile. Since, in the anomalous dispersion regime, soliton propagation in the form of a hyperbolic secant shape is known to be supported in an optical fiber [12], the envelope shape of the experimental FWM spectrum was investigated. It was found that at the output of 50 m of fiber the spectral envelope could be fit by a hyperbolic secant shape. However, these experiments were performed in the normal dispersion regime, where the fundamental soliton shape is predicted to be a hyperbolic tangent. Furthermore, in the normal dispersion regime, true solitons are essentially dips in a continuous wave carrier. Theoretical and experimental research indicates that solitonlike pulses can be supported on carrier pulses where the length of stable propagation in the fiber is determined by the length of the carrier [16]. Further studies need to be done to determine if the FWM processes in the fiber evolved to a train of stable soliton dips in the long-pulse background for the fiber lengths investigated in the experiments [33].

The experimental results pointed to the need to modify the approach to the theoretical modeling of the four-wave-mixing processes. The experimental measurements tracing the sideband evolution along the fiber length showed that the different first-order sidebands evolved with different dynamics. This observation was not accounted for in the standard theoretical models. By imposing an asymmetry on the spectral structure of the pump inputs, the sidebands were found to follow different dynamical evolutions. Specifically, one of the pump inputs was modeled to consist of two closely spaced longitudinal modes. It is worth emphasizing that the intermode spacing is very small compared to the difference in wavelength of the two pump lasers, is not resolvable with the spectrometer system used, and had to be resolved with a higher-resolution wavemeter. This multimode input was found to alter the sideband dynamics dramatically.

The experimental measurements of the sideband power with length along the fiber indicated that there was damping of the periodic evolution of sideband power with increasing fiber length. Again, this was not accounted for by the standard theory. One interpretation that gives insight into the damping of the sidebands is that the exchange of power between the pumps and sidebands copropagating in the fiber can be thought of as a coherent process. The experimental measurements showed the damping of sideband power, indicating that there was a mechanism along the fiber acting to remove the coherence of the power exchange between the pumps and sidebands. This mechanism was modeled by adding weak phase fluctuations to the waves as they propagated along the fiber, using the continuous-wave model (coupled amplitude equations). These phase fluctuations were found to account for the damping of the sideband power evolution along the fiber. However, the physical source of these phase fluctuations has yet to be determined and is an area for future research. Numerical simulations using the present approach, including a multimode input and phase fluctuations along the fiber length, were performed for the parameters of the experiments and excellent quantitative and qualitative agreement was found.

ACKNOWLEDGMENTS

D.L.H. and R.R. acknowledge support from the Division of Chemical Sciences, Office of Basic Energy Sciences, the Office of Naval Research, and National Science Foundation (Grant No. NCR-961225). We thank Patrick O'Shea for his comments on the manuscript. D.L.H. thanks Jerry Zadnik for his assistance with the GTRI CCD camera.

[1] G. P. Agrawal, *Nonlinear Fiber Optics* (Academic, San Diego, 1989).
[2] R. H. Stolen, E. P. Ippen, and A. R. Tynes, Appl. Phys. Lett. **20**, 62 (1972); E. P. Ippen and R. H. Stolen, *ibid.* **21**, 539 (1972); R. G. Smith, Appl. Opt. **11**, 2489 (1972).
[3] R. H. Stolen, J. Opt. Soc. Am. B **41**, 191 (1986).
[4] R. H. Stolen and A. Ashkin, Appl. Phys. Lett. **22**, 294 (1973).
[5] R. H. Stolen and C. Lin, Phys. Rev. A **17**, 1448 (1978).
[6] M. N. Islam, L. F. Mollenauer, R. H. Stolen, J. R. Simpson, and H. T. Shang, Opt. Lett. **12**, 625 (1987).
[7] A. Hasegawa and F. D. Tappert, Appl. Phys. Lett. **23**, 142 (1973).
[8] L. F. Mollenauer, R. H. Stolen, and J. P. Gordon, Phys. Rev. Lett. **45**, 1095 (1980).

[9] K. Smith and L. F. Mollenauer, *Optical Solitons—Theory and Experiment*, edited by J. R. Taylor (Cambridge University Press, Cambridge, 1992), p. 1.
[10] R. L. Fork, C. H. Brito Cruz, P. C. Becker, and C. V. Shank, Opt. Lett. **12**, 483 (1987).
[11] E. Udd, Rev. Sci. Instrum. **66**, 4015 (1995).
[12] A. Hasegawa, *Optical Solitons—Theory and Experiment* (Ref. [9]).
[13] J. R. Thompson and R. Roy, Phys. Rev. A **43**, 4987 (1991).
[14] S. Trillo, S. Wabnitz, and T. A. B. Kennedy, Phys. Rev. A **50**, 1732 (1994).
[15] J. R. Thompson and R. Roy, Phys. Rev. A **44**, 7605 (1991).
[16] Y. S. Kivshar, IEEE J. Quantum Electron. **29**, 250 (1993).
[17] T. R. Taha and M. J. Ablowitz, J. Comput. Phys. **55**, 231 (1984); **72**, 501 (1987).
[18] J. R. Thompson, Ph.D. dissertation, Georgia Institute of Technology, 1991 (unpublished).
[19] D. L. Hart, A. Judy, T. A. B. Kennedy, R. Roy, and K. Stoev, Phys. Rev. A **50**, 1807 (1994).
[20] Y. Chen, J. Opt. Soc. Am. B **7**, 43 (1990).
[21] W. H. Press, S. A. Teukolsky, W. T. Vetterling, and B. P. Flannery, *Numerical Recipes in C*: *The Art of Scientific Computing* (Cambridge University Press, Cambridge, 1992).
[22] D. A. Marcuse, J. Lightwave Technol. **9**, 121 (1991).
[23] R. H. Stolen, W. Pleibel, and J. R. Simpson, J. Lightwave Technol. **2**, 639 (1984).
[24] B. E. Burke, R. W. Mountain, P. J. Daniels, and D. C. Harris, Opt. Eng. (Bellingham) **26**, 890 (1987); B. E. Burke, R. W. Mountain, D. C. Harris, M. W. Bautz, J. P. Doty, G. R. Ricker, and P. J. Daniels, IEEE Trans. Electron Devices **38**, 1069 (1991).
[25] J. C. Twichell, B. E. Burke, R. K. Reich, W. H. McGonagle, C. M. Haung, M. W. Bautz, J. P. Doty, G. R. Ricker, R. W. Mountain, and V. S. Dolat, Rev. Sci. Instrum. **61**, 2744 (1990).
[26] J. A. Zadnik, Ph.D. dissertation, Georgia Institute of Technology, 1993 (unpublished).
[27] A. C. Newell and J. V. Moloney, *Nonlinear Optics* (Addison-Wesley, Reading, MA, 1992).
[28] D. Marcuse, *Theory of Dielectric Optical Waveguides*, 2nd ed. (Academic, San Diego, 1991).
[29] F. Reitmayer and E. Schuster, Appl. Opt. **11**, 1107 (1972).
[30] J. M. De Freitas and M. A. Player, Appl. Phys. Lett. **66**, 3552 (1995).
[31] G. Vemuri and R. Roy, Opt. Commun. **77**, 318 (1990); R. F. Fox, I. R. Gatland, R. Roy, and G. Vemuri, Phys. Rev. A **38**, 5983 (1988).
[32] H. Risken, *The Fokker-Planck Equation* (Springer-Verlag, Berlin, 1989).
[33] C. S. West and T. A. B. Kennedy, Phys. Rev. A **47**, 1252 (1990); T. A. B. Kennedy (unpublished).